A crystal plasticity investigation of slip system interaction, GND density and stored energy in non-proportional fatigue in Nickel-based superalloy

Xu Lu[1], Fionn P.E. Dunne[1] and Yilun Xu[1*]

[1]Department of Materials, Imperial College London, London SW7 2AZ, UK

Abstract

A dislocation and gradient-based crystal plasticity finite element study of fatigue has been carried out for nickel-based superalloy RR1000 in order to investigate detrimental non-proportional effects on fatigue life. Six differing multiaxial loading cycles including both proportional and non-proportional paths have been addressed and a critical stored energy density criterion employed for fatigue life. Non-proportional paths are shown to lead to higher numbers of intragranular slip system activations, reflecting experimental observations. These give higher geometrically necessary dislocation (GND) densities resulting from slip system interaction occurring through latent hardening effects in the model. The higher GND densities in turn drive up local stress and stored energy densities, thereby leading to lower predicted fatigue lives, in keeping with non-proportional fatigue experiments in the alloy considered. Intragranular slip system interaction may be the mechanistic explanation for non-proportional effects in fatigue of engineering alloys.

Keywords: multiaxial fatigue, non-proportional loading, life prediction, crystal plasticity; nickel-based superalloy;

* Corresponding author: Yilun Xu email: yilun.xu@imperial.ac.uk

1 Introduction

Engineering components often undergo fatigue loading, but failure must be avoided particularly in relation to safety-critical plant. To avoid economic disadvantage and loss of life, there remains a clear need to establish fully mechanistic understanding of fatigue and the ability to quantitatively predict fatigue lifetime under multiaxial loading conditions.

Nickel-based superalloys have been widely used in aerospace, vehicle and power industries for their excellent properties of high strength under high temperature and corrosion resistance. Transition metals Cr, Co, W, Zr are common alloying elements for nickel-based superalloys used in advanced turbine engines. To provide optimum mechanical properties, powder metallurgy processing routes have been introduced for these alloys including nickel-based superalloy RR1000, which is the focus of this study.

It has been widely acknowledged that non-proportional loading, where applied multiaxial stress components are not in proportion to one another, is more harmful than proportional loading in fatigue [1–4]. However, the mechanisms leading to the degradation of fatigue lifetime remain unclear. This paper therefore addresses non-proportionality in fatigue damage. We assess the role of non-proportionality in driving multiple slip system activation, together with lattice curvature development and hence geometrically necessary dislocation density which we show to result from intra-grain slip system interactions. The latter in turn are shown to establish local high

stored energy densities which have been shown in previous work [5,6] to drive fatigue crack nucleation.

There are several approaches reported in the literature to quantify non-proportionality of cyclic loading paths. Phase angle [7,8] is the most common with respect to sinusoidal loading histories, while the direction of principal stress and stress amplitude ratio [9–11] are also used to characterize non-proportionality. For arbitrary loading paths, some universally applicable measures [2,12–15] were developed based on the geometric features of the applied path itself. In general, non-proportionality leads to fatigue life decrease compared to equivalent proportional fatigue [16,17]. This can potentially be understood from the aspect of multi-slip system interactions. The activation of intra-grain slip and multiple slip system activations were observed in RR1000 after cyclic loading as shown in Figure 1 [18]. Another study [19] found that intragranular multi-slip activation in fatigue is observed more frequently with non-proportionality, shown in Figure 2. Studies [20] on deformation mechanisms of nickel alloys show evidence that GND densities concentrate where activated slip systems interact (Figure 3). Although high GND density due to strain gradient [21] is not always associated with fatigue crack nucleation, it contributes to the accumulation of local stored energy which has been linked to crack nucleation [6]. Thus, we hypothesise that intragranular multi-slip activation under non-proportional loading may be responsible for the decreasing fatigue life, due to the local high GND densities and stored energy densities caused by intra-grain slip systems interaction.

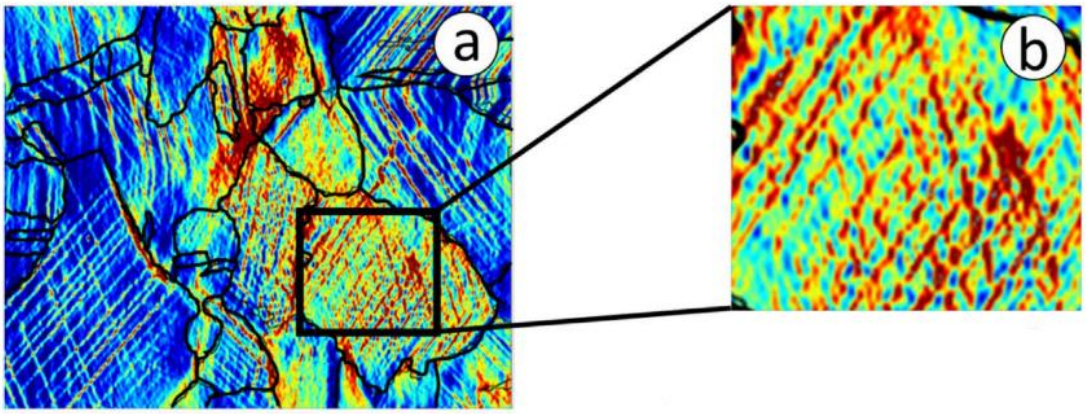

Figure 1. DIC measurement shows (a) Strain map for RR1000 after cyclic loading. (b) Multiple slip system activation in a single grain [18].

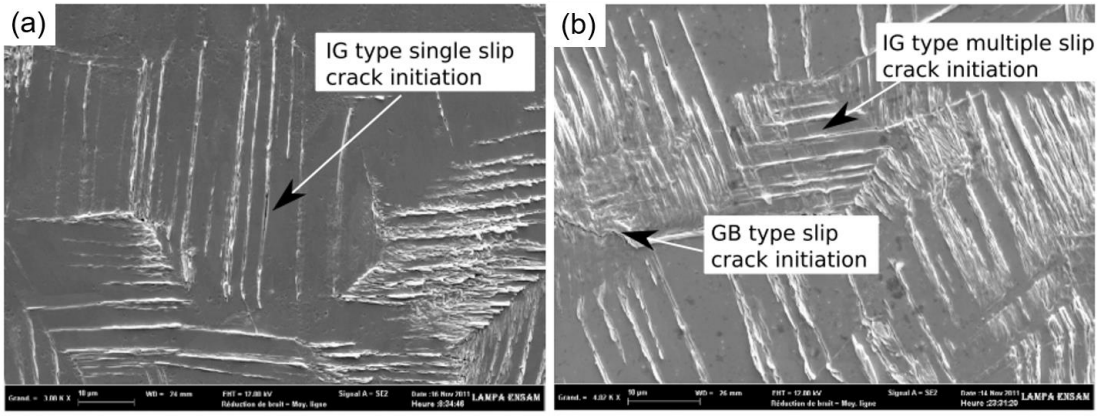

Figure 2. SEM observation of pure copper after 10^6 cycles under (a) torsion loading and (b) combined tension-torsion non-proportional loading [19].

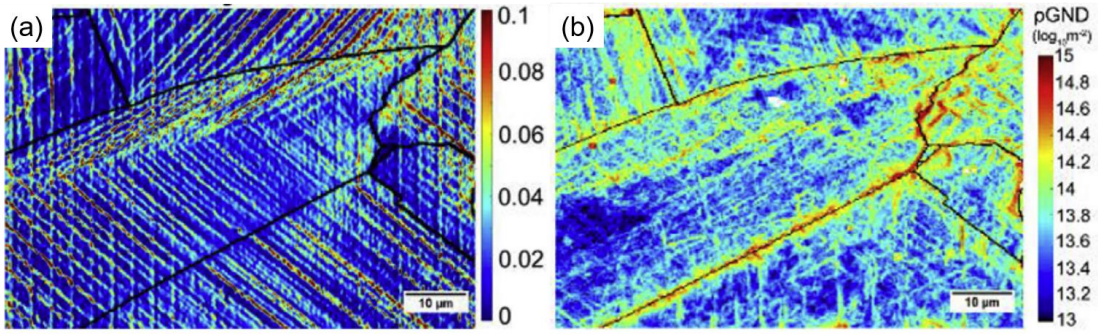

Figure 3. (a) HR-DIC result of Nitronic 60 showing xx strain map. (b) HR-EBSD GND density map of the same grain [20].

In the present paper, we employ gradient-enhanced, dislocation-based crystal plasticity modelling to investigate non-proportional fatigue in nickel alloy RR1000. The role of non-proportional loading in activating multiple slip systems is assessed, together with the resulting intra-granular slip system interaction which occurs relative

to that for proportional loading. The lattice curvatures and corresponding GND densities which support them are quantified and these together with the local slip accumulations and stresses are used to determine the local stored energy densities. The latter have been shown to provide good estimates of fatigue performance [22] such that it then becomes possible to explore the mechanistic basis for fatigue behaviour under non-proportionality of loading. We show that the primary driver of reduced fatigue lives in non-proportional loading in RR1000 is multi-slip system interactions driving high GND densities and stored energies over those which occur in equivalent proportional loading. In what follows, a brief description of the crystal plasticity methodology is provided for RR1000, and the polycrystal model and non-proportional loading conditions presented. Quantitative investigations of intra-grain multi-slip, GND density, stored energy and fatigue lives under proportional and non-proportional loading are then addressed which are followed by discussion and conclusions.

2 Methodology

2.1 Crystal plasticity finite element modelling

A gradient-enhanced, dislocation-based crystal plasticity slip rule [23] is employed in order to capture independent slip system activation, statistically stored (SSD) and geometrically necessary (GND) dislocation densities.

The plastic velocity gradient $\boldsymbol{L}^{\mathrm{p}}$ is determined from crystal slip rates $\dot{\gamma}^{\alpha}$ on the α^{th} slip system by

$$\boldsymbol{L}^{\mathrm{p}} = \dot{\boldsymbol{F}}^{\mathrm{p}} \boldsymbol{F}^{\mathrm{p}-1} = \sum_{\alpha=1}^{12} \dot{\gamma}^{\alpha} \, \boldsymbol{s}^{\alpha} \otimes \boldsymbol{n}^{\alpha} \tag{1}$$

where $\boldsymbol{s}^{\alpha}$ and $\boldsymbol{n}^{\alpha}$ are the slip and plane normal directions of slip plane of the α^{th} slip system respectively. The slip rate $\dot{\gamma}^{\alpha}$ is given by

$$\dot{\gamma}^{\alpha} = \rho_{\text{ssdm}} \nu b^2 \exp\left(-\frac{\Delta F}{k\text{T}}\right) \sinh\left(\frac{\Delta V}{k\text{T}} |\tau^{\alpha} - \tau_c^{\alpha}|\right) \quad (2)$$

in which ρ_{ssdm} is the mobile dislocation density, b the Burgers vector magnitude, k the Boltzman's constant, ν the frequency of dislocation escape attempts at obstacles with energy barrier ΔF, and ΔV the corresponding activation volume. T is the temperature, which here remains constant at 293 K. τ^{α} is the resolved shear stress acting on slip system α and τ_c^{α} the corresponding critical resolved shear stress (CRSS).

Geometrically necessary dislocations (GNDs) resulting from lattice curvature and consequently plastic strain gradients are discussed by Ashby [24] and Seeger [25]. Statistically stored dislocations (SSDs), which result in zero net open Burgers circuit, evolve during plastic deformation and are discussed by Kocks [26]. Both SSDs and GNDs contribute to slip system hardening and this is incorporated in the slip system behaviour by leading to an increase in intrinsic slip system strength by

$$\tau_c^{\alpha} = \tau_{c0}^{\alpha} + Gb\sqrt{\rho_{\text{GND}} + \rho_{\text{SSD}}} \quad (3)$$

in which τ_{c0}^{α} is the initial critical resolved shear stress (CRSS), G the shear modulus, and ρ_{SSD} and ρ_{GND} the SSD and GND densities respectively. The rate of evolution of SSD density is taken to evolve linearly with the effective plastic strain rate $\dot{p}$ and given by

$$\dot{\rho}_{SSD} = \lambda \dot{p} \quad (4)$$

where λ is the hardening coefficient. Hence all slip systems harden isotropically such that there is a latent hardening effect in which the activation of single slip during one stage of the non-proportional loading path causes the (latent) hardening of the other non-activated systems. In a subsequent part of the loading history (at a point of load direction change, for example), a different slip system may be activated but which has already undergone hardening from the earlier part of the cycle. This gives rise to potentially very differing responses from proportional and non-proportional loading paths.

The effective plastic strain rate $\dot{p}$ is related to the plastic deformation rate

$$\dot{p} = (\frac{2}{3}\boldsymbol{D}^{\mathrm{p}}\colon \boldsymbol{D}^{\mathrm{p}})^{1/2} \tag{5}$$

which is obtained from the plastic velocity gradient

$$\boldsymbol{D}^{\mathrm{p}} = \mathrm{sym}(\boldsymbol{L}^{\mathrm{p}}) \tag{6}$$

The density of GNDs ρ_{GND} is determined from the Nye dislocation tensor which is related to the local plastic strain gradients supporting the lattice curvature. Because of the potential non-unique relationship between the lattice curvature and the GND density, the latter is calculated using an L2-norm minimization method [27,28] from

$$\rho_{\mathrm{GND}} = \sqrt{{\rho_{\mathrm{Gs}}}^2 + {\rho_{\mathrm{Get}}}^2 + {\rho_{\mathrm{Gen}}}^2} \tag{7}$$

where ρ_{Gs} is the sum of slip system GND screw components and ρ_{Get} and ρ_{Gen} are the sum of the edge components. These are computed from Nye's dislocation tensor which is related to plastic strain gradients by

$$\boldsymbol{\Lambda} = \mathrm{curl}(\boldsymbol{F}^{\mathrm{p}}) = \sum_{\alpha=1}^{12}(\rho_{Gs}^{\alpha}\,\boldsymbol{b}^{\alpha}\otimes\boldsymbol{m}^{\alpha} + \rho_{Get}^{\alpha}\boldsymbol{b}^{\alpha}\otimes\boldsymbol{t}^{\alpha} + \rho_{Gen}^{\alpha}\boldsymbol{b}^{\alpha}\otimes\boldsymbol{n}^{\alpha}) \tag{8}$$

The slip and hardening rules above are implemented within a user-defined material subroutine (UMAT) using ABAQUS standard analysis.

2.2 Material properties

Slip rule properties and parameters used to capture the behaviour of Ni-based alloy RR1000 are listed in Table 1, which have been determined by Chen [22] based on multi-axial load-controlled fatigue test results provided by Rolls-Royce. The 12 octahedral slip systems relevant to RR1000 alloy (FCC crystal structure) are illustrated in Appendix A. Cubic slip is argued to be unlikely to be relevant to this material at the temperature considered.

Table 1. Slip rule properties and parameters [22]

ρ_{ssdm}(μm^{-2})	b(μm)	ν(s^{-1})	ΔF(J)	k(J K^{-1})	T(K)
0.05	3.51×10^{-4}	1×10^{11}	3.46×10^{-20}	1.38×10^{-23}	293
τ_{c0}(MPa)	G (MPa)	λ(μm^{-2})	ΔV		
450	90×10^{3}	150	$37.5b^3$		

2.3 Geometric model generation

A polycrystal representative volume element (RVE) model with 144 grains was generated using VGrain [29] to emulate the microstructure of fine-grained polycrystalline RR1000, as shown in Figure 4(a). Independent studies indicate that this is capable of representing material behaviour with reasonable integrity [30]. Set of random Euler angles were generated using MATLAB in order to give an RVE model with random-textured microstructure as indicated by the pole figure in Figure 4(b). The polycrystal finite element model was meshed with three element sizes, 0.5 μm, 0.75 μm and 1 μm respectively, using three-dimensional, 20-noded quadratic

hexahedral elements with reduced integration (C3D20R). The polycrystal model, together with representative loading and boundary conditions, are shown schematically in Figure 4(c). Distributed loading on the top free surface facilitated the application of direct and shear stresses to the polycrystal. The region of interest (ROI) in Figure 4(a) indicates that within which subsequent microstructure-level results were extracted in order to minimise boundary effects.

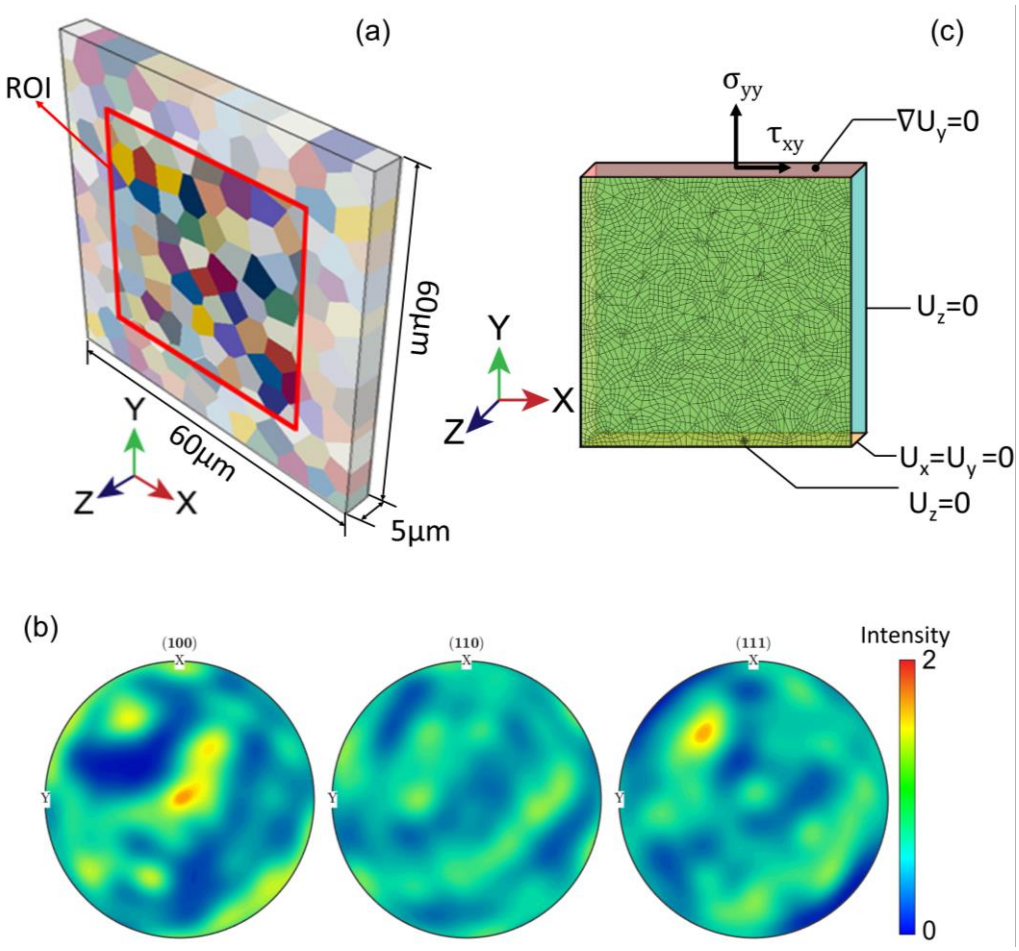

Figure 4. Schematic diagrams of (a) the FEM model and the region of interest, (b) pole figure displaying the random-textured microstructure of the model, and (c) boundary conditions and finite element mesh shown on the polycrystal model front free surface .

Strain-controlled uni-axial loading was applied to the polycrystal firstly for the three differing element sizes in order to investigate the mesh refinement sensitivity. Figure

5(a) gives the frequency distribution of accumulated plastic strain after loading and Figure 5(b) the average, macroscale stress-strain curves. The model with mesh size 0.75µm exhibits a sufficiently close strain distribution as the one with mesh size 0.5µm, and the difference of macroscopic stress between the models with mesh size 0.75µm and 0.5µm is shown to be less than 1.5% at strain level 1% in Figure 5(b). Hence, an element size of 0.75 µm was chosen for subsequent calculations giving approximately 120 elements within each grain.

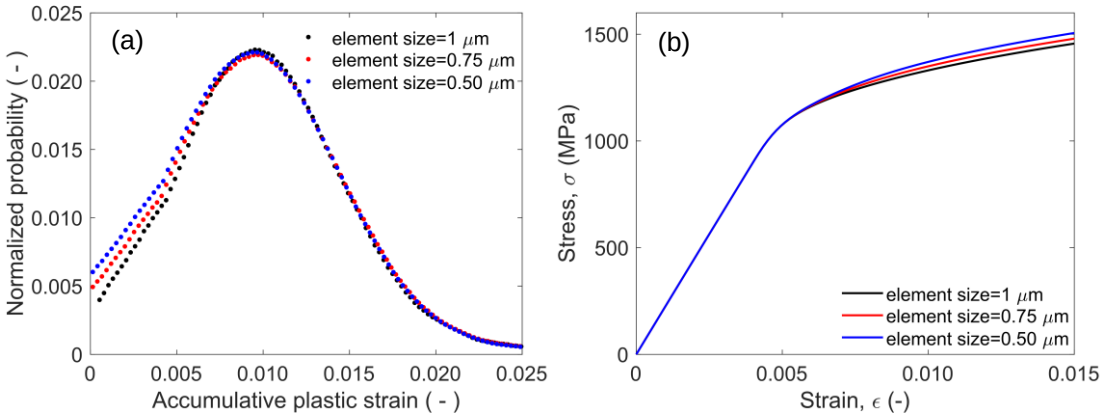

Figure 5. (a) Frequency distribution of accumulative plastic strain and (b) the engineering stress-strain curves after single stretch with element size of 1 µm, 0.75 µm and 0.50 µm.

Three levels of peak applied (von Mises effective) stress were selected in this study, with the lowest of 1050 MPa being close to the yield stress, and the two others being 1200 and 1350 MPa. For each peak applied Mises stress level, the polycrystal model was assigned six differing loading paths, all with stress ratio of R = -1, under conditions of uniaxial direct and shear stress, the latter being simple shear loading. The respective peak Mises effective stresses applied for the set of loading paths was unchanged for each of the three peak stress conditions. Figure 6 shows the three proportional and three non-proportional loading paths chosen, which include pure axial stress and shear stress loading as well as mixed loading. Other studies [6,31] have shown that

the first few cycles are generally adequate to reveal the heterogeneity of the deformation at the microstructural level, and other key characteristics of the fatigue process (for example, the locations of highest slip accumulation, stress, GND density and stored energy density), such that in this study, results are obtained after 20 cycles.

In order to characterize the applied loading path, a shear index expressed by

$$S(t) \equiv |\tau(t)| \Big/ \left(\frac{1}{\sqrt{3}}\sigma_e(t)\right) \tag{9}$$

is utilised, in which τ and σ_e are the shear and Mises effective stresses respectively at time t, indicating the strength of the applied shearing with respect to the overall applied load.

Phase angle [7,8] has been used to quantify the non-proportionality of multiaxial loading with sinusoidal loading histories, defined as the shift angle between zero points of two alternating quantities. Therefore, in this paper, the non-proportionality is simply defined by phase difference, similar to the phase angle, given by

$$\varphi \equiv |t_\sigma - t_\tau|/T \tag{10}$$

where $|t_\sigma - t_\tau|$ is the difference between the instant of first peak of axial stress and that of shear stress, and T is the period of a loading cycle, and is calculated for each loading cycle considered in Figure 6.

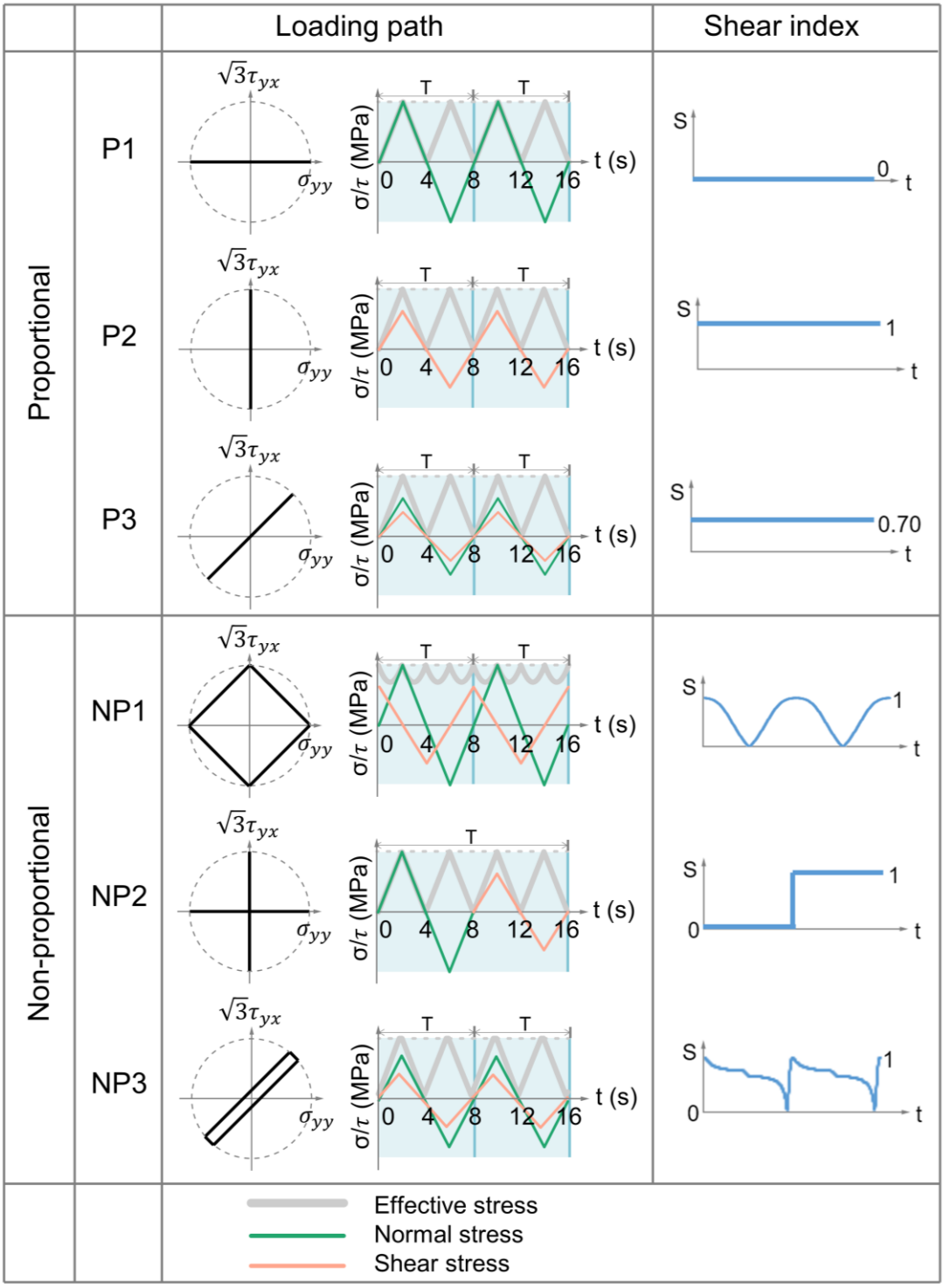

Figure 6. Schematics of applied loading paths and corresponding shear indices and phase differences.

2.4 Stored energy density criterion for fatigue crack nucleation

The stored energy density criterion used in this study to predict fatigue lifetime was proposed by Wan [5]. This quantity has been used successfully to identify both crack nucleation site and to predict the cycles required in order to nucleate the fatigue crack. It is based on the idea that at the crystal slip level, dislocations pile up and form structures, with which are associated a dislocation configurational energy. The length scale over which this energy is stored is that associated with the dislocation structure and in turn is the length scale at which the stress becomes high enough, in the absence of slip in locked dislocation structures, to cause new free surfaces and hence crack nucleation. Hence a configurational energy *density* is determined per unit area, over a length scale given by the dislocation density [32]. Discrete dislocation studies have shown that the dislocation configuration energy density can be reasonably well captured at the crystal level. A critical energy density is determined for crack nucleation [33] prediction.

The stored energy generated per cycle which is associated with plastic deformation is obtained as a fraction of the plastic work

$$\dot{U} = \int |\boldsymbol{\sigma} : \mathrm{d}\boldsymbol{\varepsilon}^{\mathrm{p}}| \tag{11}$$

The relevant volume over which the energy is stored before crack nucleation is given by

$$\Delta V_s = \lambda' \Delta A_s = \frac{\Delta A_s}{\sqrt{\rho_{\mathrm{GND}} + \rho_{\mathrm{SSD}}}} \tag{12}$$

where ΔV_s is the storage volume, ΔA_s the potential free surface area generated, and λ' the mean free spacing of immobile dislocations and finally, the stored energy density per cycle ($\dot{G}$, Jm^{-2}) can be calculated by

$$\dot{G} = \frac{\dot{U}\Delta V_s}{\Delta A_s} = \int \frac{\zeta |\boldsymbol{\sigma} : d\boldsymbol{\varepsilon}^{\mathrm{p}}|}{\sqrt{\rho_{GND} + \rho_{SSD}}} \tag{13}$$

in which ζ refers to the fraction of dissipated energy stored as dislocation structures whose value is not known exactly but is often estimated to be ~0.05 [34,35] while the remaining plastic energy is dissipated in the form of heat.

As argued by Littlewood et al. [36,37], the evolution of GNDs and SSDs as well as slip accumulation, is rapid in the first few fatigue cycles, and reaches a steady stage with a stable and constant growth rate after a few cycles. Hence, the stored energy after a few cycles of loading can be expressed approximately by

$$G = G_{\mathrm{i}} + \int \dot{G}_{\mathrm{ss}} \, \mathrm{d}N \tag{14}$$

where G_{i} refers to the stored energy density after the first i (typically 20) cycles, $\dot{G}_{\mathrm{ss}}$ is the steady state cyclic stored energy density rate, and N is the number of fatigue cycles following the achievement of steady state at i cycles. A critical stored energy density G_{c} is specified for a given material, thereby enabling the number of fatigue cycles to achieve the critical stored energy density and crack nucleation to be determined.

3 Results

3.1 Accumulative plastic strain

The proportional (labelled P) and non-proportional (NP) loading conditions shown in Figure 7 were applied to the polycrystal model shown in Figure 7 over 20 fatigue cycles

and at the three (Mises effective) peak stress levels shown. They result in heterogeneous distributions of slip accumulation as shown in Figure 7 after 20 fatigue cycles. The first clear observation is that non-proportional loadings NP1, NP2 and NP3 together with proportional (simple shear) loading P2 lead to the highest accumulations of plastic strain. The proportional simple shear loading (P2) leads to much higher strain accumulation, for given applied Mises stress, than the proportional direct loading (P1). The highest local strains developing for NP1, NP2 and P2 arise in the same location in the microstructure. Path NP3 is indicatively the least non-proportional of NP1-NP3 and leads to low predicted accumulated strain, at a level similar to proportional path P3, but a little higher.

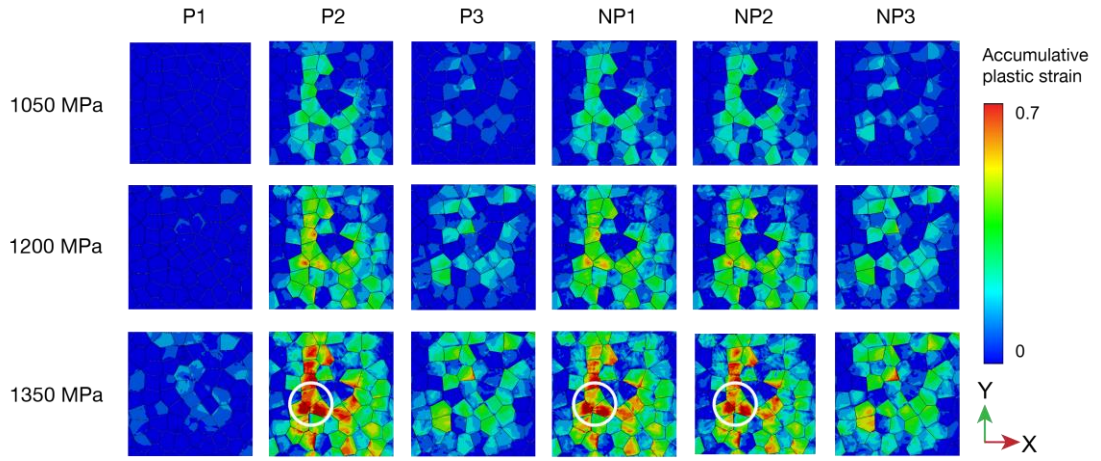

Figure 7. Contour plots of accumulative plastic strain for the 6 loading paths and 3 effective stress levels shown after 20 fatigue cycles. Grains with the highest plastic strains are highlighted (by circles) for the case of peak effective applied stress of 1350 MPa.

3.2 Activated slip systems and GND densities

The numbers of activated slip systems within each grain were assessed under the differing loading conditions, and the frequency distributions for the lowest peak applied stress (1050 MPa) are shown in Figure 8(a). The non-proportional loading

paths can be seen to activate more slip systems; the shear paths P2 and NP2 give rise to similar slip system activations because the level of non-proportionality in NP3 is really quite low but nonetheless, a higher fraction of grains can be seen to be activated by the non-proportionality even in this case. Figure 8(b) shows the average number of activated slip systems within the polycrystal RVE. The numbers activated for non-proportional paths NP1 and NP2 are substantially higher than any of the proportional paths, and NP3 leads to a small but consistent increase in numbers activated compared to proportional loading P3.

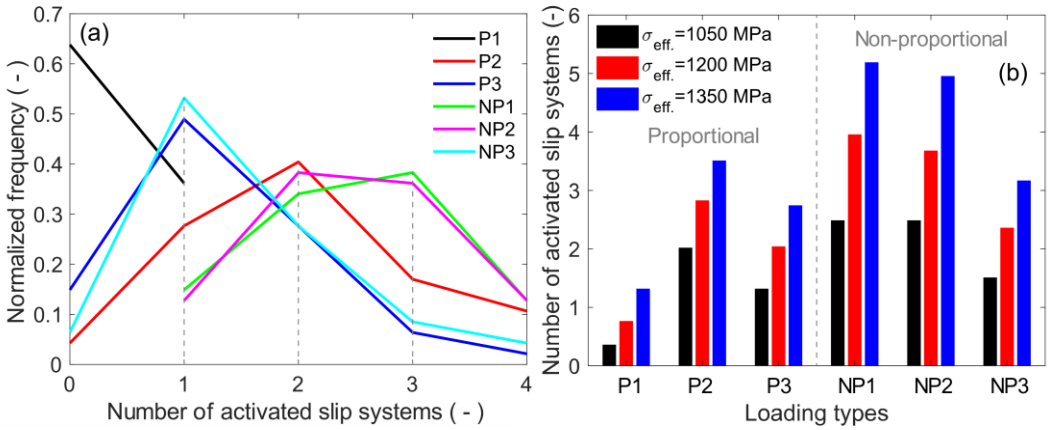

Figure 8. (a) Granular frequency distribution of number of slip systems activated after 20 cycles for each loading path with peak applied effective stress of 1050 MPa, (b) average number of activated slip systems for each loading path after 20 fatigue cycles.

Zhao et al [20] observed experimentally the intra-granular interaction of differing activated slip systems and quantified the local GND densities developed with high resolution electron backscatter diffraction (HR-EBSD) measurements in an austenitic Nitronic 60 steel. Their work was carried out for monotonic deformation but provided the interesting result that the slip system interactions resulted in substantively higher local densities of GNDs. It is well acknowledged experimentally [19] that non-proportional loading leads to higher numbers of slip system activations, and the

polycrystal model results in Figure 9 above reassuringly reproduce this conclusion. Non-proportional fatigue loading therefore leads to higher numbers of slip system activations and consequently, potentially to higher numbers of interactions and hence to higher GND densities. This is the contention in this paper and is important because if it can be established that higher GND densities result from non-proportional loading due to intra-granular slip system interactions, then so higher local stored energies are developed leading to shorter fatigue lives. Non-proportional fatigue in metal polycrystals is well-established in the literature to give shorter fatigue lives but the mechanistic basis has not yet been presented. Hence in this paper, we next investigate the role of non-proportionality in driving higher GND densities at interacting slip systems.

We consider loading path NP1 with peak applied stress of 1350 MPa, since it resulted in the greatest number of activated slip systems. Figure 9 shows the predicted GND density spatial distribution. Two grains (G1 and G2) with low GND densities and two (G3 and G4) with high GND densities have been highlighted for comparison. Sub-figures show the intra-granular plastic strains together with details of the crystal orientations, and the activated slip systems. The grains developing high GND densities are found to be those undergoing multi-slip and conversely, it's the single-slip grains leading to low GND density. Multi-slip gives rise to slip system interactions which result in strong plastic strain gradients and to high lattice curvature, and hence to high local GND densities. The latter potentially leads to high stored energy density in turn reducing cycles to nucleate fatigue cracks.

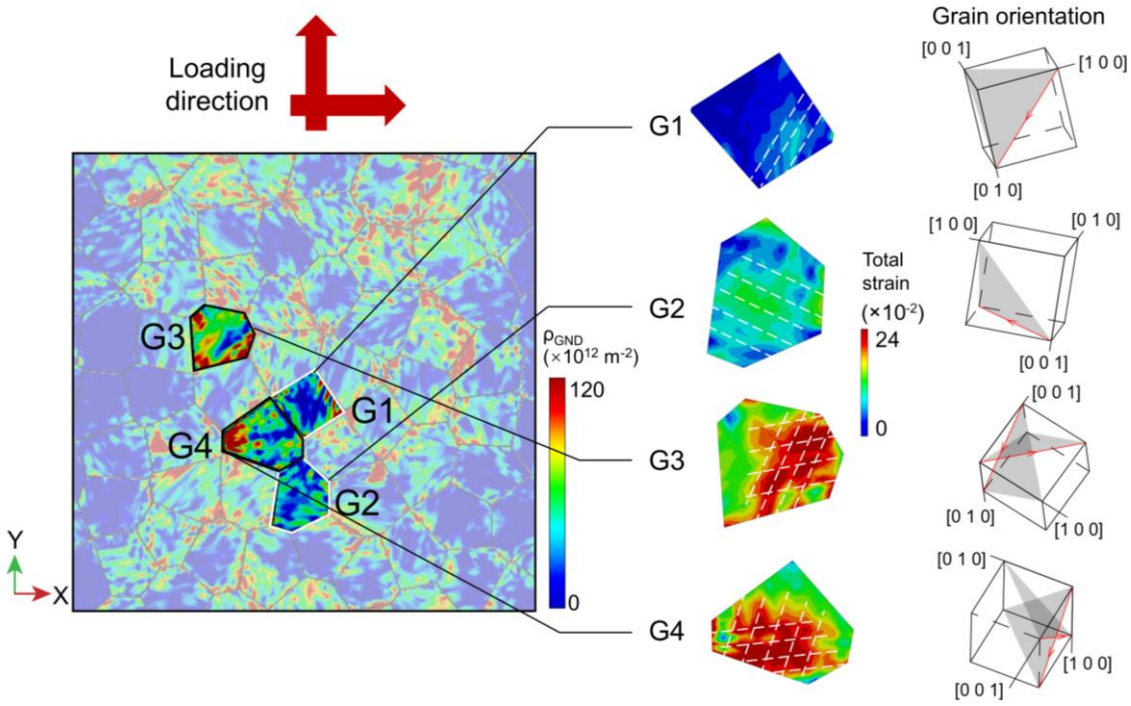

Figure 9. GND distribution resulting after 20 cycles of loading path NP1 with applied peak stress 1350 MPa, and sub-figures showing intra-granular (effective) strain within two (single slip) grains (G1, G2) with low GND density and two (double slip) grains (G3, G4) with high GND density. Intra-granular activated slip systems are shown in both the contour plots (white broken lines) and the crystal lattice schematics (red lines) showing the grain orientations.

Further quantitative assessment is given in Figure 10 which shows the spatial predicted GND density distribution within grains G2 and G4 (see Figure 9) within the polycrystal. Path A-A' through G2 and G4 is shown along which the distribution of GND density is extracted in order to compare the results obtained for non-proportional versus proportional loading paths. Firstly, Figure 10(a-d) shows the GND density distributions obtained for two proportional and two non-proportional loading paths. The activated slip systems are highlighted for each grain. Slip systems that are activated under different proportional loading paths separately are all activated under non-proportional paths. In addition, the distribution of GND density along path A-A' is plotted in Figure 10(e, f), showing higher GND densities for non-proportional loading

paths, as well as higher GND densities in G4, where more slip systems were activated, than for that in G2.

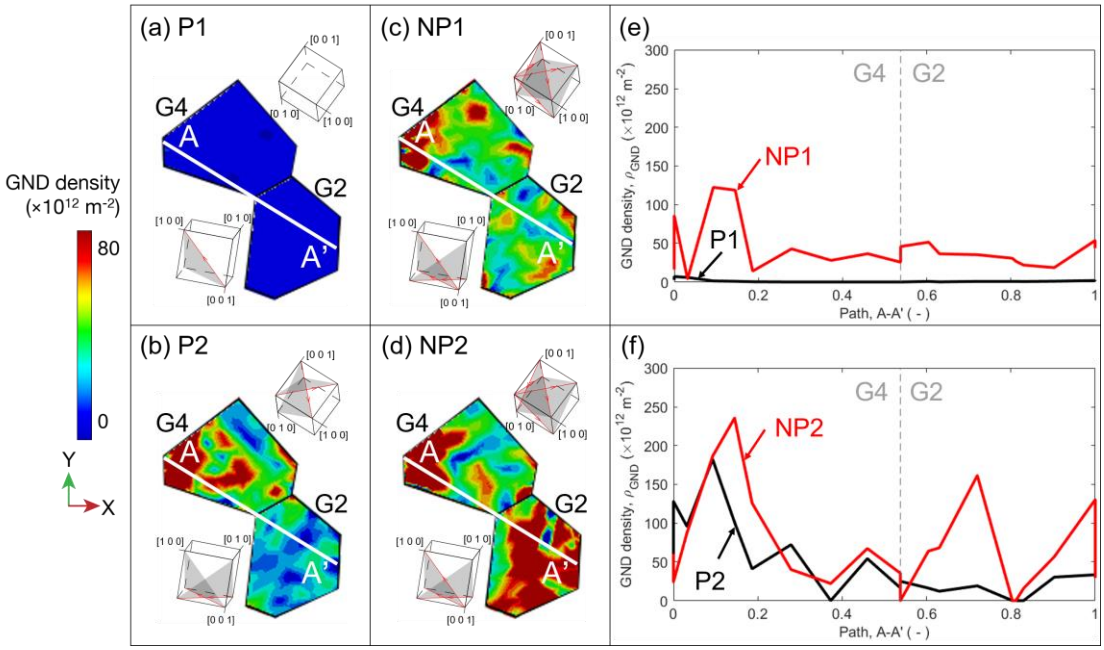

Figure 10. (a-d) GND maps of G2 and G4 (see Figure 9) under peak applied stress of 1350 MPa for the loading paths indicated, with insets showing activated slip systems; and GND development along path A-A' for (e) cycles P1, NP1 and (f) cycles P2, NP2.

The GND density frequency distributions in Figure 11 also shows higher GND densities resulting from the non-proportional paths in the whole region of interest (see Figure 4(a)), confirming that this phenomenon is not confined to particular grain selections, but in fact is maintained for the polycrystal response overall. Combined with the average number of activated slip systems shown in Figure 8(b), it is reasonable to argue that multiple slip activation is the driver of higher local and polycrystal average GND density.

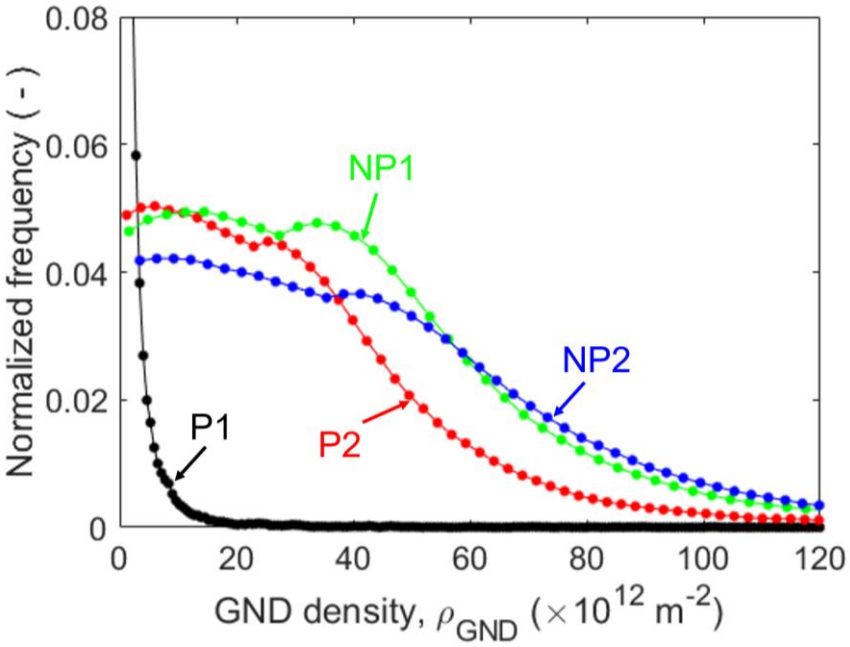

Figure 11. Frequency distributions of GND density calculated over the complete polycrystal ROI for loading paths P1, P2, NP1, and NP2 after 20 cycles for peak applied stress level of 1350 MPa.

Of all the loading paths, P3 and NP3 have the smallest difference in level of non-proportionality, as given by Eqn.(9) and the phase difference in Figure 6. It is therefore of interest to investigate the consequences of low levels of non-proportionality for plastic strain, GND density and stored energy density (and hence fatigue life). Results are shown in Figure 12 for loading paths P3 and NP3. Line path B-B' is chosen to include the point of highest stored energy density in both cases P3 and NP3. The results again reveal generally higher strains, GND densities and stored energy densities under non-proportional loading, even for the very low level of non-proportionality in path NP3. The key quantity associated with fatigue life, the stored energy density cyclic evolution, is higher for the non-proportional loading such that with further fatigue cycling, the critical stored energy would be achieved earlier than that for the proportional loading, leading to shorter fatigue life in the former. This is investigated next for all the proportional and non-proportional loading paths considered.

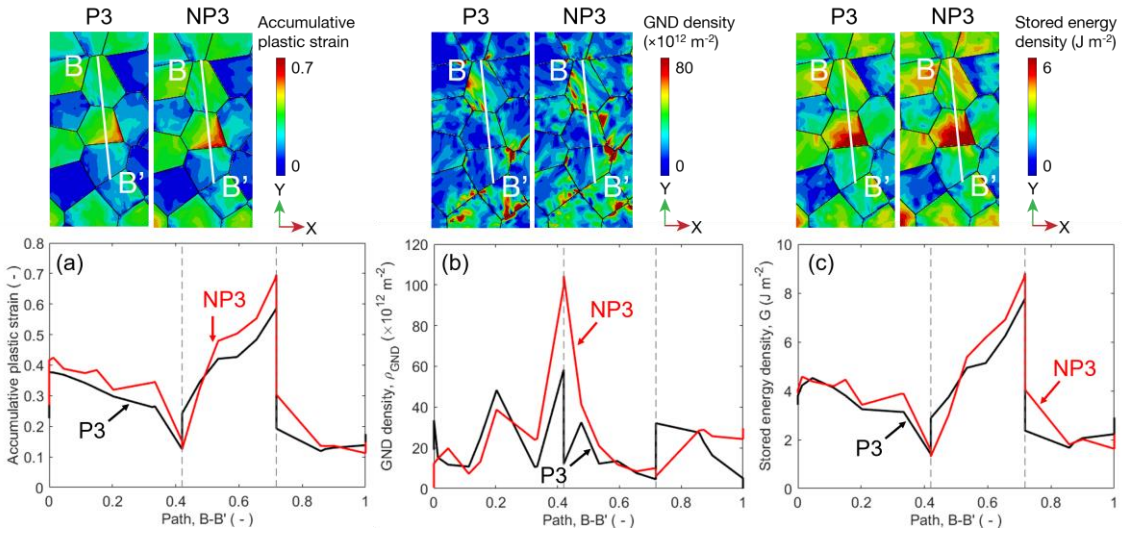

Figure 12. Fields of (a) accumulative plastic strain, (b) GND density, and (c) stored energy density along path B-B' after 20 cyclic loadings for loading paths P3 and NP3 with peak applied effective stress of 1350 MPa

3.3 Development of stored energy density and predicted fatigue lifetime

Considering loading path NP1 first, Figure 13(a) shows the development of stored energy density within the polycrystal ROI, and along path C-C' through four key grains, during the first 20 cycles. The highest stored energy density occurs at the same position within the microstructure after about the 15th cycle and subsequently remains at this location. That is, the location within the microstructure at which the rate of accumulation of stored energy density is highest may change in the early cycles of loading because of the plasticity, the SSD and GND hardening, and the resulting redistribution of stress. However, the stored energy density distribution (along with that for other key microstructural quantities) develops rapidly in the first and subsequent few cycles until a stabilized cyclic development is established. This is reflected in the progressive distributions shown in Figure 13(b). Stress hotpots are also found near grain boundaries, contributing to the concentration of stored energy at these locations, which potentially leads to crack initiation at these locations. However,

previous experimental and numerical work [6,33] has reported that stress is a necessary but not sufficient criterion for ductile fatigue crack initiation.

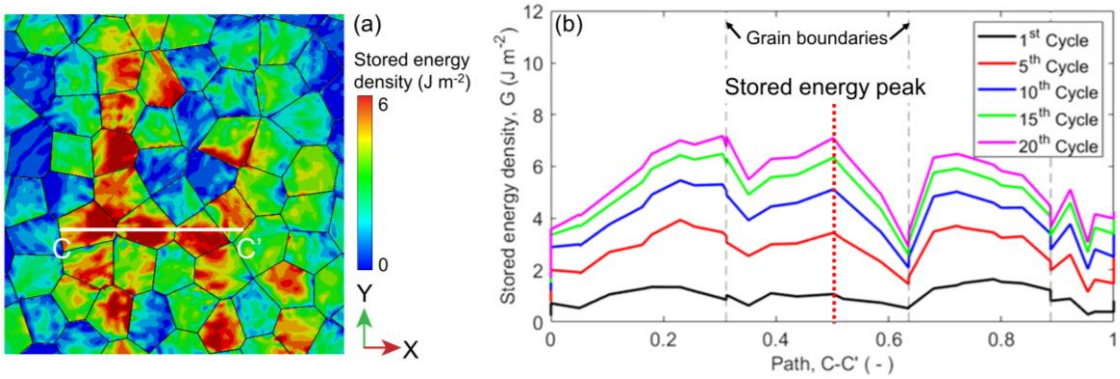

Figure 13. (a) The field distribution of stored energy density after 20 cycles, and (b) development of stored energy density along path C-C' under loading path NP1, with applied peak effective stress of 1350 MPa.

The values of peak stored energy density at the end of each cycle for all loading paths were extracted over 20 loading cycles, and the results are plotted in Figure 14(a-c) for the three applied peak effective stresses. A critical stored energy density for RR1000 has previously been determined to be 404 J m^{-2} [22]. Stored energy densities increase rapidly in the first few cycles as discussed above until an approximately steady rate is achieved, as depicted in Figure 14(a-c). The methodology presented in Section 2.4 (Eqn (14)) is utilised in order to determine the predicted number of cycles required to nucleate a fatigue crack for each of the loading conditions and paths, taking the above critical stored energy density for fine-grained RR1000. The recent study [38] has proved the validity of stored energy density criterion to predict fatigue lifetimes, compared to the experimental evidence provided by Janssens [8]. The resulting predicted S-N (peak stress versus cycles to failure) curves are shown in Figure 14(d). An approximately linear relationship is seen to arise between applied peak σ_{eff} and $\log_{10} N_f$. The longest fatigue lifetimes are observed to be predicted for proportional,

axial loading (P1) while the non-proportional path NP1 results in the fewest cycles to failure, and substantive differences in fatigue life are predicted. The three non-proportional paths result in the lowest lifetimes but proportional loading paths P2 and P3 also have relatively short lives compared to axial loading path P1. The simple shear loading path, P2, gives the shortest life of the three proportional paths, and comes closest to that of the non-proportional paths.

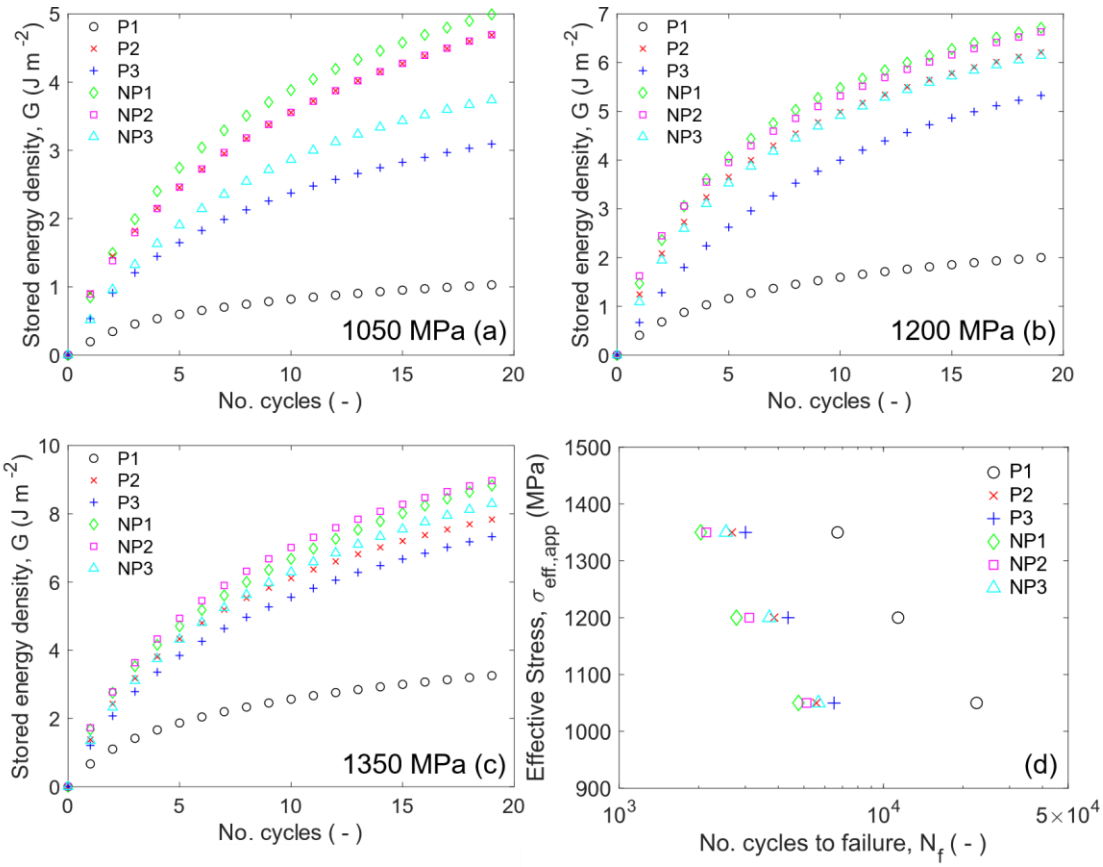

Figure 14. Stored energy densities versus cycles for all loading paths shown for applied peak stresses of (a) 1050 MPa, (b) 1200 MPa, and (c) 1350 MPa. Applied peak stress against predicted fatigue lifetime is shown in (d).

4 Conclusion

Non-proportional and proportional fatigue in fine-grained RR1000 were investigated using dislocation and gradient-based crystal plasticity incorporating geometrically necessary dislocation evolution and latent slip system hardening. Non-proportional

paths are predicted generally to lead to shorter fatigue lifetimes (reflecting experiments) compared with proportional cycling for the following mechanistic reasons.

- Increasingly non-proportional loading paths drive higher numbers of intragranular slip system activations, resulting in higher accumulated straining.
- Multiple intragranular slip system activations lead to slip system interactions which are captured in the modelling through latent hardening effects, which reflect the higher GND densities developed by the multi-slip system interaction.
- The higher GND densities and resulting stresses lead to increased local stored energy densities which result in lower predicted fatigue lives. Intragranular slip system interaction may therefore be the mechanistic explanation for non-proportional effects in fatigue detriment of engineering alloys. This would need to be established (or otherwise) by further experimental and quantitative characterisation studies.

Acknowledgement

FPED wishes to acknowledge gratefully the provision of Royal Academy of Engineering/Rolls-Royce research chair funding.

Appendix A

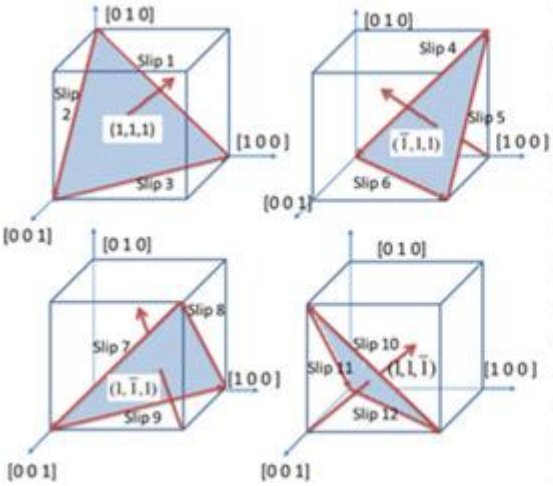

Slip system	Slip plane normal	Slip direction
1	$(1,1,1)$	$[1,\bar{1},0]$
2	$(1,1,1)$	$[0,1,\bar{1}]$
3	$(1,1,1)$	$[1,0,\bar{1}]$
4	$(\bar{1},1,1)$	$[1,1,0]$
5	$(\bar{1},1,1)$	$[0,1,\bar{1}]$
6	$(\bar{1},1,1)$	$[1,0,1]$
7	$(1,\bar{1},1)$	$[1,1,0]$
8	$(1,\bar{1},1)$	$[0,1,1]$
9	$(1,\bar{1},1)$	$[1,0,\bar{1}]$
10	$(1,1,\bar{1})$	$[1,\bar{1},0]$
11	$(1,1,\bar{1})$	$[0,1,1]$
12	$(1,1,\bar{1})$	$[1,0,1]$

Figure A1. Identification of FCC slip directions and normals, and slip direction number designations utilized throughout the paper, shown with respect to an orthogonal (x, y, z) reference system.

Reference

[1] Hamada N, Sakane M, Itoh T, Kanayama H. High temperature nonproportional low cycle fatigue using fifteen loading paths. Theor Appl Fract Mech 2014;73:136–43. https://doi.org/10.1016/j.tafmec.2014.07.006.

[2] Zhong B, Wang Y, Wei D, Zhang K, Wang J. Multiaxial fatigue life prediction for powder metallurgy superalloy FGH96 based on stress gradient effect. Int J Fatigue 2018;109:26–36. https://doi.org/10.1016/j.ijfatigue.2017.12.006.

[3] Itoh T, Yang T. Material dependence of multiaxial low cycle fatigue lives under non-proportional loading. Int J Fatigue 2011;33:1025–31. https://doi.org/10.1016/j.ijfatigue.2010.12.001.

[4] Lu C, Melendez J, Martínez-Esnaola JM. A universally applicable multiaxial fatigue criterion in 2D cyclic loading. Int J Fatigue 2018;110:95–104. https://doi.org/10.1016/j.ijfatigue.2018.01.013.

[5] Wan VVC, MacLachlan DW, Dunne FPE. A stored energy criterion for fatigue crack nucleation in polycrystals. Int J Fatigue 2014;68:90–102. https://doi.org/10.1016/j.ijfatigue.2014.06.001.

[6] Chen B, Jiang J, Dunne FPE. Is stored energy density the primary meso-scale mechanistic driver for fatigue crack nucleation? Int J Plast 2018;101:213–29. https://doi.org/10.1016/j.ijplas.2017.11.005.

[7] Paul SK. Prediction of non-proportional cyclic hardening and multiaxial fatigue life for FCC and BCC metals under constant amplitude of strain cycling. Mater Sci Eng A 2016;656:111–9. https://doi.org/10.1016/j.msea.2016.01.029.

[8] Janssens KGF. Proportionally and non-proportionally perturbed fatigue of stainless steel. Int J Fatigue 2018;110:42–8. https://doi.org/10.1016/j.ijfatigue.2017.12.013.
[9] Li J, Zhang ZP, Sun Q, Li CW. Multiaxial fatigue life prediction for various metallic materials based on the critical plane approach. Int J Fatigue 2011;33:90–101. https://doi.org/10.1016/j.ijfatigue.2010.07.003.
[10] Lu C, Melendez J, Martínez-Esnaola JM. Modelling multiaxial fatigue with a new combination of critical plane definition and energy-based criterion. Int J Fatigue 2018;108:109–15. https://doi.org/10.1016/j.ijfatigue.2017.12.004.
[11] Li BC, Jiang C, Han X, Li Y. A new approach of fatigue life prediction for metallic materials under multiaxial loading. Int J Fatigue 2015;78:1–10. https://doi.org/10.1016/j.ijfatigue.2015.02.022.
[12] Zhong B, Wang Y, Wei D, Wang J. A new life prediction model for multiaxial fatigue under proportional and non-proportional loading paths based on the pi-plane projection. Int J Fatigue 2017;102:241–51. https://doi.org/10.1016/j.ijfatigue.2017.04.013.
[13] Bees MR, Pattison SJ, Fox N, Whittaker MT. The non-proportional behaviour of a nickel-based superalloy at room temperature, and characterisation of the additional hardening response by a modified cyclic hardening curve. Int J Fatigue 2014;67:134–41. https://doi.org/10.1016/j.ijfatigue.2014.02.023.
[14] de Freitas M, Reis L, Li B. Comparative study on biaxial low-cycle fatigue behaviour of three structural steels. Fatigue Fract Eng Mater Struct 2006. https://doi.org/10.1111/j.1460-2695.2006.01061.x.
[15] de Freitas M. Multiaxial fatigue: From materials testing to life prediction. Theor Appl Fract Mech 2017;92:360–72. https://doi.org/10.1016/j.tafmec.2017.05.008.
[16] Shang D-G, Sun G-Q, Chen J-H, Cai N, Yan C-L. Multiaxial fatigue behavior of Ni-based superalloy GH4169 at 650°C. Mater Sci Eng A 2006;432:231–8. https://doi.org/10.1016/j.msea.2006.06.014.
[17] Yu Q, Zhang J, Jiang Y, Li Q. Multiaxial fatigue of extruded AZ61A magnesium alloy. Int J Fatigue 2011;33:437–47. https://doi.org/10.1016/j.ijfatigue.2010.09.020.
[18] Mello AW, Nicolas A, Sangid MD. Fatigue strain mapping via digital image correlation for Ni-based superalloys: The role of thermal activation on cube slip. Mater Sci Eng A 2017;695:332–41. https://doi.org/10.1016/j.msea.2017.04.002.
[19] Agbessi K, Saintier N, Palin-Luc T. Microstructure-based study of the crack initiation mechanisms in pure copper under high cycle multiaxial fatigue loading conditions. Procedia Struct. Integr., vol. 2, Elsevier B.V.; 2016, p. 3210–7. https://doi.org/10.1016/j.prostr.2016.06.400.
[20] Zhao C, Stewart D, Jiang J, Dunne FPE. A comparative assessment of iron and cobalt-based hard-facing alloy deformation using HR-EBSD and HR-DIC. Acta Mater 2018;159:173–86. https://doi.org/10.1016/j.actamat.2018.08.021.
[21] Xu Y, Balint DS, Dini D. A new hardness formula incorporating the effect of source density on indentation response: A discrete dislocation plasticity analysis. Surf Coatings Technol 2019;374:763–73.

https://doi.org/10.1016/j.surfcoat.2019.06.045.
[22] Xu L, Pang JHL. Nano-indentation characterization of Ni–Cu–Sn IMC layer subject to isothermal aging. Thin Solid Films 2006;504:362–6. https://doi.org/10.1016/j.tsf.2005.09.056.
[23] Dunne FPE, Rugg D, Walker A. Lengthscale-dependent, elastically anisotropic, physically-based hcp crystal plasticity: Application to cold-dwell fatigue in Ti alloys. Int J Plast 2007;23:1061–83. https://doi.org/10.1016/j.ijplas.2006.10.013.
[24] Ashby MF. The deformation of plastically non-homogeneous materials. Philos Mag A J Theor Exp Appl Phys 2006;21:399–424. https://doi.org/10.1080/14786437008238426.
[25] Seeger A. Crystal plasticity theory during the 1950s and 1960s. Philos Mag 2013;93:3772–94. https://doi.org/10.1080/14786435.2013.822998.
[26] Kocks UF. A statistical theory of flow stress and work-hardening. Philos Mag 1966;13:541–66. https://doi.org/10.1080/14786436608212647.
[27] Cheng J, Ghosh S. A crystal plasticity FE model for deformation with twin nucleation in magnesium alloys. Int J Plast 2015;67:148–70. https://doi.org/10.1016/J.IJPLAS.2014.10.005.
[28] Arsenlis A, Parks DM. Crystallographic aspects of geometrically-necessary and statistically-stored dislocation density. Acta Mater 1999. https://doi.org/10.1016/S1359-6454(99)00020-8.
[29] Zhang P, Balint D, Lin J. An integrated scheme for crystal plasticity analysis: Virtual grain structure generation. Comput Mater Sci 2011;50:2854–64. https://doi.org/10.1016/j.commatsci.2011.04.041.
[30] Yeratapally SR, Glavicic MG, Hardy M, Sangid MD. Microstructure based fatigue life prediction framework for polycrystalline nickel-base superalloys with emphasis on the role played by twin boundaries in crack initiation. Acta Mater 2016;107:152–67. https://doi.org/10.1016/j.actamat.2016.01.038.
[31] Jiang J, Yang J, Zhang T, Dunne FPE, Britton T Ben. On the mechanistic basis of fatigue crack nucleation in Ni superalloy containing inclusions using high resolution electron backscatter diffraction. Acta Mater 2015;97:367–79. https://doi.org/10.1016/j.actamat.2015.06.035.
[32] Zheng Z, Prastiti NG, Balint DS, Dunne FPEE. The dislocation configurational energy density in discrete dislocation plasticity. J Mech Phys Solids 2019;129:39–60. https://doi.org/10.1016/j.jmps.2019.04.015.
[33] Prastiti NG, Xu Y, Balint DS, Dunne FPE. Discrete dislocation, crystal plasticity and experimental studies of fatigue crack nucleation in single-crystal nickel. Int J Plast 2020;126:102615. https://doi.org/10.1016/j.ijplas.2019.10.003.
[34] Kamlah M, Haupt P. On the Macroscopic Description of Stored Energy and Self Heating During Plastic Deformation. Int J Plast 1997;13:893–911. https://doi.org/10.1016/S0749-6419(97)00063-6.
[35] Hodowany J, Ravichandran G, Rosakis AJ, Rosakis P. Partition of plastic work into heat and stored energy in metals. Exp Mech 2000;40:113–23. https://doi.org/10.1007/BF02325036.
[36] Littlewood PD, Wilkinson AJ. Geometrically necessary dislocation density distributions in cyclically deformed Ti-6Al-4V. Acta Mater 2012;60:5516–25.

https://doi.org/10.1016/j.actamat.2012.07.003.
[37] Littlewood PD, Wilkinson AJ. Local deformation patterns in Ti–6Al–4V under tensile, fatigue and dwell fatigue loading. Int J Fatigue 2012;43:111–9. https://doi.org/https://doi.org/10.1016/j.ijfatigue.2012.03.001.
[38] Chen B, Jansenss K, Dunne FPE. Role of geometrically necessary dislocation density in multiaxial and non-proportional fatigue crack nucleation. Int J Fatigue 2020:105517. https://doi.org/https://doi.org/10.1016/j.ijfatigue.2020.105517.